

Raman scattering by carbon nanotubes coupled to quantum dots via dipolar excitonic interaction

Anna Wroblewska,[†] Niclas Sven Mueller,[‡] Mariusz Zdrojek,[†] Stephanie Reich,[¶]
and Georgy Gordeev^{*,¶,§}

[†]*Faculty of Physics, Warsaw University of Technology, Koszykowa 75, 00-662, Warsaw, Poland*

[‡]*NanoPhotonics Centre, Cavendish Laboratory, Department of Physics, JJ Thompson Avenue, University of Cambridge, Cambridge, CB3 0HE, United Kingdom*

[¶]*Department of Physics, Freie Universität Berlin, 14195 Berlin, Germany*

[§]*Department of Physics and Materials Science, University of Luxembourg, L-4422 Belvaux, Luxembourg*

E-mail: georgy.gordeev@uni.lu

Abstract

The dipole-dipole interactions between excitons are of paramount importance in the nanoscale structures. When two excitons are placed together they can exchange the energy can manifest in the resonant Raman cross sections. We provide theoretical framework for such effects by combining the coupled oscillator model and perturbation theory. We apply this theory to a hybrid film comprising semiconducting quantum dots and metallic carbon nanotubes. The quantum dots exciton has a fixed energy, while the nanotube resonances span across a larger range from 1.7 to 1.93 eV. We acquire the resonant Raman profiles of the pristine nanotubes and hybrids and find a relative shift between them. The shift direction depends on the relative energies between the CNT and QD exciton energies, as predicted by our theory.

Introduction

Many bosonic particles can be represented by a dipole, including phonons, plasmons, or excitons. These particles can interact via a dipole-dipole (dd) mechanism which can yield new hybrid forms such as plexitons or can be arranged into dipolar lattices.^{1,2} The dd interaction between two excitons can result in Davydov splitting observed molecular crystals³⁻⁵ and can facilitate dipolar moiré crystals.⁶ Nanoscale systems from 0D to 2D typically host excitonic effects due to low screening and can be engineered into novel dipolar hybrids. However, the optical methods to study exciton-exciton interactions remain limited. The standard techniques as scattering and absorption spectroscopies frequently used for plexitons⁷⁻⁹ and molecular crystals³⁻⁵ fail for multi-component systems as they only probe the resonance of the entire system. Förster energy transfer is limited to the direct-band-gap semiconductors and can be probed only by emission of the lowest energy state.¹⁰⁻¹³ To advance dipolar hybrids discovery and applications, one requires new methods that are element-specific and work for higher-energy states and non-emitting materials.

Resonant Raman spectroscopy (RRs) is widely applied to study direct band gap excitons in semiconducting and semi-metallic systems.^{14,15} RRs probes excitonic energies and lifetimes via exciton-phonon coupling^{16,17} and signals can be easily distinguished by their characteristic Raman fingerprint.¹⁸ Compared to linear light spectroscopy within the Raman process exciton-photon interaction occurs twice when photon is absorbed and emitted. When the exciton is represented by a Lorenz oscillator and its dipole coupling is captured by a coupled oscillator model, frequently used for phonon-phonon,¹⁹⁻²¹ exciton-plasmon^{22,23} dipolar couplings. Nevertheless, the microscopic description of the Raman process that incorporates the coupled oscillator model for two excitons has been missing as well its experimental demonstration.

For probing exciton-exciton coupling effects we need an experimental platform that allows close proximity of two systems but prevents wavefunction mixing that produces additional effects. For example, spacer-free Van der Waals bilayers and core-shell quantum dots (QDs)

exhibit charge-transfer states and are not suitable. We propose a mixed dimensional system where zero dimensional QDs and 1D single-walled carbon nanotubes (CNTs) are introduced into a thin film. Recently we achieved an assembly free from nanoparticle ligands as well as CNTs surfactants,²⁴ that allows close proximity of nanoparticles and nanotubes. Further CNTs represent provide excitonic states in large spectral range that can report energy dependent effects. The assembly of quantum dots with the same type of core-shell materials provide a constant excitonic level with high oscillator strength. Further a choice of metallic CNT chiralities can suppresses strong PL signal from QDs that otherwise covers Raman signals.

In this work, we explore the resonant Raman effects of the dd coupling. First we formulate the Raman scattering process with excitons coupled via dipolar mechanism. We probe this experimentally in films containing metallic CNTs of mixed chiralities and InP/ZnS quantum dots. The CNT excitons below the QD resonance experience a red shift, and those above the QD resonance experience a blue shift in agreement with our theory. We discuss the strength of the coupling between QD and CNT, as well as the collective dipolar QD-QD coupling.

Experimental methods and samples

Vacuum filtration method was used to produce homogenous hybrid CNT - InP/ZnS films. The suspensions of pure metallic carbon nanotubes were dissolved in a 1% solution of sodium dodecyl sulfate (SDS) surfactant from thick film carbon nanotubes (NanoIntegris). The mixture was then sonicated for 5 hours and centrifuged at 8000 rpm for 10 minutes to obtain a stable and clear solution. Nanocrystals InP/ ZnS (MkNano, 1 mg/ml) and diluted to a concentration of 0.01 mg/ml. To prepare each sample 3.5 ml of carbon nanotube solution was used and mixed with InP/ZnS nanocrystals in volumes respectively: 0.5 ml, 1 ml and 2 ml (later marked as: InP1, InP2, InP3). The mixture of carbon nanotubes and nanocrystals was heated in 50°C for 30 min and sonicated for 30 min. Each of the prepared mixtures was

placed in a filter funnel and filtered through a cellulose filter (Merc Millipore, diameter 25 mm, pore size 25 nm). The exact procedure of the vacuum filtration process is presented in our previous manuscript.²⁴ The layer was transferred from the cellulose filter to a Si/SiO₂ substrate by using acetone vapour bath for 30 min and put in warm acetone bath for 15 min. In the last stage, the sample was placed in isopropanol solution for 3 min. Prepared samples were tested with SEM imaging (Figure 3a and Supplementary Figures X-X). Samples have InP/ZnS nanocrystals in the whole volume of the thin film. The thickness of the samples were ≈ 50 nm (AFM measurement).

Topography monitoring was performed using a Raith e-Line plus electron microscope to produce SEM images and control residues and impurities. Thickness of the films was analyzed with Bruker Icon atomic force microscope. Optical spectroscopy was acquired with PerkinElmer LAMBDA 850 + UV/vis spectrometer equipped with a 150 mm Integrating Sphere for optical absorbance measurement.

Results and discussion

Theory of dipole-dipole altered Raman scattering

The coupling between the CNT and QD excitons can be formulated with a dipole-dipole coupling approach. As model we use mechanically coupled damped oscillators, whose motion is described by the set of two equations:^{22,23}

$$\begin{aligned} \frac{d^2\mu_{QD}(t)}{dt^2} + \omega_{QD}^2\mu_{QD}(t) + \gamma_{QD}\frac{d\mu_{QD}(t)}{dt} &= A_{QD} [E_0\cos(\omega t) + M_c\mu_{CNT}] \\ \frac{d^2\mu_{CNT}(t)}{dt^2} + \omega_{CNT}^2\mu_{CNT}(t) + \gamma_{CNT}\frac{d\mu_{CNT}(t)}{dt} &= A_{CNT} [E_0\cos(\omega t) + M_c\mu_{QD}] \end{aligned} \quad (1)$$

The μ_X is the dipole moment with $X = CNT, QD$. A is related to the oscillator strength. γ is the damping factor inversely proportional to the exciton lifetime. M_c is a matrix element, representing the coupling. ω is the oscillation frequency.

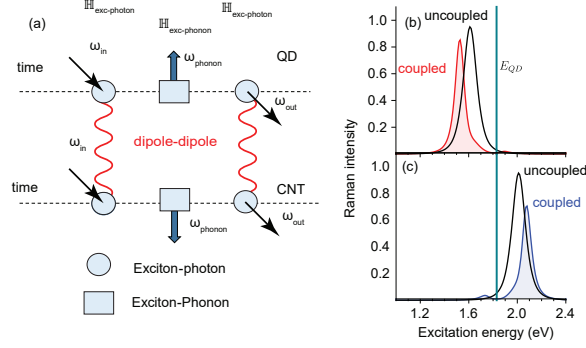


Figure 1: Dipole-dipole coupling in Raman scattering. (a) Feynman diagram Raman scattering processes with dipole-dipole coupling included. The tilted arrows represent photons ($\omega_{in}, \omega_{out}$), where interaction occurring at round vertices. The vertical blue arrows indicate the interaction with the phonon. The red line interconnects the QD and CNT excitons with dipole-dipole coupling. (b) Resonance Raman profiles computed with Eq. (5) when $E_{CNT} < E_{QD}$, set as 1.6 and 1.8 eV, respectively, black line is uncoupled ($M_c = 0$) and red line is coupled system ($M_c = 10$ eV). Panel (c) is same as (b) for $E_{CNT} > E_{QD}$, $E_{CNT} = 2$ eV.

The solutions of Eq. (1) can be used to deduce the exciton-photon coupling elements, which include dipole-dipole coupling. From steady state solutions of Eq. (1) we obtain the new dipole moments of the CNT at the stationary regime

$$\mu_{CNT}^0 = \frac{E_0 A_{CNT} \left[1 + \frac{A_{QD}}{B_{QD}(\omega)} \right]}{B_{CNT} \left[1 - \frac{A_{QD} A_{CNT} M_c^2}{B_{QD}(\omega) B_{CNT}(\omega)} \right]} = E_0 \frac{A_{CNT}^{eff}}{B_{CNT}} \quad (2)$$

where the $B_X = (\omega_X^2 - \omega^2 - i\omega\gamma_X)$. The expression $\frac{\mu\omega}{E_0}$ in Eq. (2) provides a modified form of the Fermi golden rule, where material absorption follows its imaginary part.

The exciton-photon matrix element $M_{ex-photon}$ can be expressed in terms of A_{CNT}^{eff} as

$$M_{ex-photon}^{eff} \propto \frac{m_e}{e(\hbar\omega_{CNT})^{0.5}} \sqrt{A_{CNT}^{eff}}, \quad (3)$$

where m_e and e is the electron effective mass and charge, respectively. We can the matrix element in Eq. (3) for Raman scattering.

A typical one-phonon Raman process is realized in the steps, see the top line in Figure 1. First the photon E_L is absorbed by pushing the exciton from ground into excited state. The

interaction occurs via exciton-photon Hamiltonian, round vertex in Figure 1. At the second step the phonon is created within the Stokes process, and the exciton is scattered into a new state $|b\rangle$. And finally the exciton relaxes back to the ground state by emitting a photon of smaller energy E_s . Without dipole-dipole interaction of the excitons the Raman scattering cross-section can be represented by the standard third-order perturbation theory:

$$I_{Raman}(E_{las}) \approx E_{las}^4 \left| \frac{M_{ex-photon} M_{ex-phonon} M_{ex-photon}}{D_{in}(\omega) D_{out}(\omega)} \right|^2, \quad (4)$$

with $D_{in,out}$ representing the denominator of the incoming and outgoing resonance $D_{in}(\omega) = (E_{las} - E_{ii} - i\gamma_{CNT})$ and $D_{out}(\omega) = (E_{las} - \hbar\omega_{phonon} - E_{ii} - i\gamma_{CNT})$. The exciton-phonon matrix element $M_{ex-phonon}$ and exciton-photon matrix $M_{ex-photon}$ are independent of excitation energy E_{las} . The E_{las}^4 dependence is given for completeness, in fact it is eliminated by the calibration procedure.

We can integrate the dd coupling effect into the perturbation theory when considering excitation energy dependent exciton-photon coupling terms. The dipole-dipole coupling occurs between the excitons at the second vertex of the Feynman diagram shown in Figure 1. The excitation energy dependence of the matrix element $M_{ex-photon}$ is driven by dipole-dipole coupling as derived in Eq. (3) and we directly introduce it into Eq. (4):

$$I_{Raman}(E_{las}) \approx E_{las}^4 \left| \frac{M_{ex-photon}^{eff}(E_{las}) M_{ex-phonon} M_{ex-photon}^{eff}(E_{las} - \hbar\omega_{phonon})}{D_{in}(\omega) D_{out}(\omega)} \right|^2, \quad (5)$$

where the $M_{ex-phonon}$ is an exciton-phonon matrix element remaining unperturbed by the dipole-dipole coupling.

Dipole-dipole coupling predicts a shift of the Raman resonance, with direction determined by the relative energy between CNT and QD excitons. Figure 1b shows changes in the resonance Raman profile after coupling is introduced in Eq. 5. The E_{CNT} is set to 1.6 eV, lower compared to the E_{QD} . In such a configuration, a red shift of the Raman resonance is expected. However, when E_{CNT} is larger than E_{QD} a blue shift of the resonance is expected,

see Figure 1. Also, the part of the energy is transferred directly from the QD, visible at a bump at 1.83 eV. The magnitude of the shift and the amount of energy transferred will depend on the system parameters in Eq. (1).

Resonant Raman cross section given by Eq. (5) can be approximated to a sum of four Raman resonances. The dipole-dipole energy transfer from the QD exciton to the CNTs exciton add an extra resonance to the intrinsic one. As a result, the CNT exciton E_{ii} splits into two parts E_{ii}^+ and E_{ii}^- . Each contribution has an incoming and an outgoing part and can be described as

$$I_{Raman}(E_{las}) \approx E_{las}^4 \left| \sum_{E_{ii}^-, E_{ii}^+} \frac{(M_{ex-photon}^{+,-})^2 M_{ex-phonon}}{(E_{las} - E_{ii}^{+,-} - i\gamma_{CNT}^{+,-})(E_{las} - \hbar\omega_{phonon} - E_{ii}^{+,-} - i\gamma_{CNT}^{+,-})} \right|^2. \quad (6)$$

In that case the matrix elements are excitation energy independent, compared to Eq. (5). The $E_{ii}^{+,-}$ can be fully resolved when phonon frequencies exceed broadening factors $\hbar\omega_{phonon} > \gamma_i$. The minimum distance between E_{ii}^+ and E_{ii}^- corresponds to the Rabi splitting of the system given as

$$2\Omega = \frac{M_c \sqrt{A_{CNT} A_{QD}}}{\omega_{QD}} \quad (7)$$

Now, we experimentally probe the dipole-dipole coupling effect in the hybrid films.

Pre-characterization

We control relative concentration between QDs and CNTs by varying the amount of initial components during vacuum filtration. We incrementally increase the QD concentration from low to high and monitor the surface of the films by scanning electron microscopy (SEM). Figure 3 shows at the bottom the pristine films without QDs. The film contains randomly oriented bundles of nanotubes, similar to previous works.²⁴ By adding a small volume of QDs we start to observe the white dotted areas on the surface of the CNT-QD-l sample,

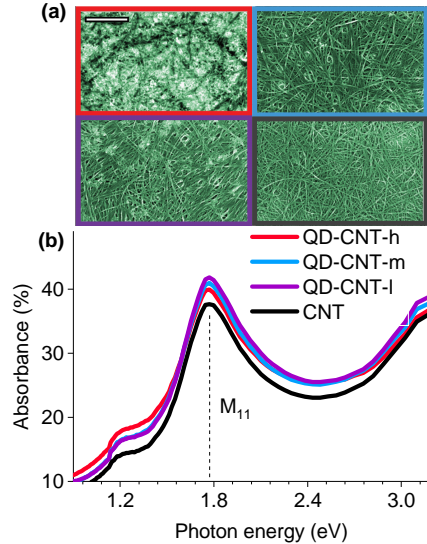


Figure 2: Characterization of the CNT-QD films. (a) SEM images from hybrids at different QDs concentrations, increasing from pristine CNTs (black) to the QD-CNT-h (red). (b) Absorption spectroscopy of films deposited on a glass substrate.

see Figure 3a (light blue). By increasing concentration of QDs up to medium and high in the CNT-QD-m, h more and more quantum dots appear in the SEM images, see Figure 3a (purple, red). Based on our previous work with CNT-gold nanoparticle system we assume the CNTs also penetrate the films.²⁴ It is important to keep the filtration speed low in order to eliminate the residues of the QD ligands, as for example shown in Supplementary Figure X. The resulting films are ≈ 50 nm thick as we estimated by atomic force microscopy.

Linear optical properties contain little insight about the coupling of CNT to the QD excitons. Figure 3b shows absorption spectra of the pristine CNTs and three QD-CNT hybrids. The optical properties are dominated by the absorption of the CNT excitons peaking near 1.8 eV. Despite the really dense QD filling, we find little change in the absorption. In the hybrids we find the changes in the absolute absorption cross section as well as slight deviations in the spectral line-shapes. We further turn to resonant Raman spectroscopy for analysis of the dipole-dipole coupling effect.

Raman spectroscopy reveals vibrational signatures of the InP/ZnS QDs inside the hybrids. Figure 3c,d shows Raman spectra acquired with 1.9 eV excitation from QD-CNT

hybrid and pristine CNTs. In the pristine film we find two sets of modes: Radial breathing modes between 150 and 200 cm^{-1} and broad intermediate frequency modes (IFM) near 450 cm^{-1} , see Figure 3d. The Radial breathing modes represent an ensemble of peaks and we analyze them in the next paragraphs. In the Raman spectrum of the QDs-CNT hybrid additional Raman modes appear; see the highlighted peaks in Figure 3b. The first (second) order of ZnS shells is found at ≈ 225 (450) cm^{-1} . These frequencies are comparable with previous studies, acquired at cryogenic temperatures.^{25,26} The InP cores are present at the 355, 381, and 405 cm^{-1} , up-shifted compared to the pure, not core/shell InPc QDs.²⁷ This is expected for core/shell QDs.²⁵ By varying laser excitation energy we can determine the energy of QD exciton E_{QD} inside the hybrid.

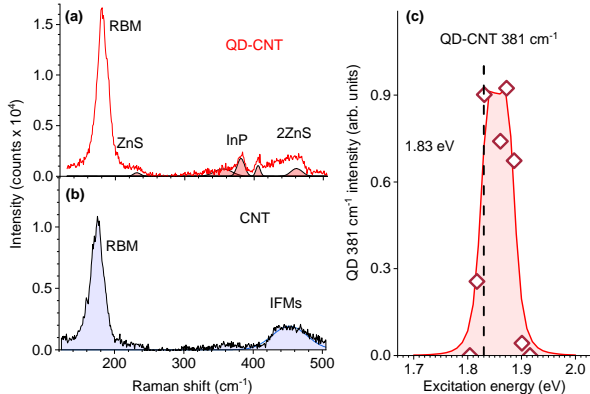


Figure 3: Resonant Raman analysis of the QDs signal (a) Raman spectrum of QD-CNT excited in resonance with quantum dots at 1.87 eV, the modes of QDs are highlighted in red. (b) Raman spectrum of the pristine CNTs, the CNT Raman peaks are highlighted in blue. (c) Resonant Raman profile of the 381 cm^{-1} Raman mode belonging to the QDs. Symbols are experimental data, line is a fit by Eq. (5). The vertical line indicates the energy of the optical transition ($E_{QD} = 1.83$, $\gamma = 20$ meV).

We quantify the energy of QDs exciton by resonant Raman spectroscopy. We analyze the Raman Raman peak at 381 cm^{-1} belonging to the InP shells, see Figure 3c. We record the Raman spectrum at several energies between 1.75 and 1.95 eV and fit the InP Raman peak with a Lorentzian function. The peak area is later divided by the area of the benzonitrile reference molecule to account for the instrumental effects; see Methods. The calibrated intensity is plotted as symbols in Figure 3d. Far from the resonance at 1.8 and 1.9 eV we

do not observe any Raman peak, indicating zero intensity. The maximum is reached in between the incoming and outgoing resonances at E_{QD} and $E_{QD} + E_{vib}$, respectively. We fit the experimental data by Eq. (4) with E_{QD} as a parameter. The fit results are shown in Figure 3d by lines, with the E_{QD} energy at 1.83 eV. Note that this energy is red-shifted from individual QDs, altered by dielectric screening²⁸ and clustering mechanisms.^{29,30} We further study the energies of excitonic transitions in CNTs.

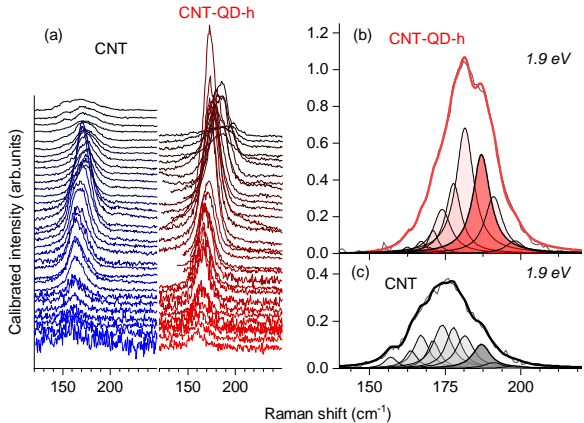


Figure 4: Analysis of the Radial breathing modes. Waterfall plot with calibrated intensity in (a) pristine and (b) QD-hybrid samples with excitation energies spanning from 1.56 (bottom) to 2 eV (top). (b,c) decomposition of the spectra excited at 1.9 eV into separate chiralities, the filled peaks represent different (n,m) species. The highlighted peak represents 187 cm^{-1} RBM.

Optical properties of the CNTs

Radial breathing modes in mixed-chirality sample contain signals from several nanotube chiralities and we need to perform chiral identification first (Fig. 4a). Figures 4b and c compare the Raman spectra of QD-CNTs-h and CNTs, respectively, both excited at 1.9 eV. At first glance it may seem that the positions of the peaks are shifting, however, that is not possible since the RBM frequency is constant and is linked to CNT diameter.³¹ Instead, we see different nanotube chiralities being in resonance. We break down the Raman spectrum into several peaks according to the Kataura plot.^{16,31} Individual RBM components are shown in Figure 4b,c. The distribution of the components and their relative intensities are different

between CNT and the CNT-QD hybrid, originating from a change in resonant conditions. We then perform the same procedure for all Raman spectra shown in Figure 4a and construct resonant Raman profiles.

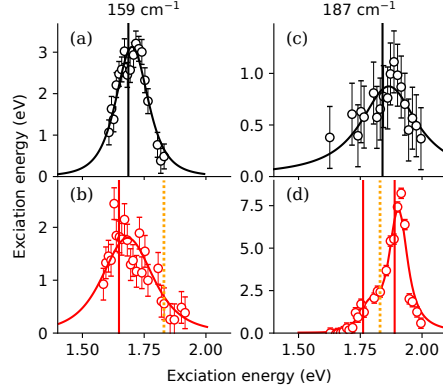


Figure 5: Resonant Raman profiles of two CNT species with exciton energy E_{CNT} below and above the QD exciton transition, the left column: the RR profile of the 159 cm^{-1} (a) without QDs and (b) with QDs (QD-CNT-h). The right column: the RR profile of the 187 cm^{-1} RBM (c) pristine and (d) QD-CNT-h. The vertical line in (b) and (d) indicates the E_{QD} at 1.83 eV.

We observe a shift of the resonant Raman profile of the CNTs in a hybrid system. At first we examine the 159 cm^{-1} . The resonant Raman profile of the pristine sample is shown in Figure 5a, using a fit with Eq. 4 we obtain a transition energy of 1.69 eV, as marked by a vertical black line. The RR profile of the hybrid system is shown in Figure 5b for the same RBM mode. We observe a red-shift of the resonance and a higher broadening, yet there is no dd transfer resonance E^+ since the QD resonance is relatively far, see vertical line in Figure 5b. We find the E^- energy by fitting the profile by Eq. (6) and find 1.69 eV. It is shifted towards lower energies by 38 meV from the pristine position, as predicted by our dd coupling theory.

The resonant Raman profile is altered by the dd coupling when the excitonic states are close in energy. We pick the RBM mode at 187 cm^{-1} highlighted in Figure 4b. Figure 5c shows RR profile of this mode in the pristine film, where we find a broad resonance with low intensity. The resonance energy is at 1.86 eV very close to the E_{QD} at 1.83 eV, and we can expect strong dd coupling effects. The RR profile of the hybrid system is shown in Figure

5d, it is up to 7.5 times more intense. Moreover it seems to be split into two parts with reduced broadening. These effects can be reproduced by the dd coupling theory.

We obtain the coupling parameter by fitting the experimental RR profiles. The line in Figure 5d represents a fit by (5) that nicely reproduces the asymmetric line-shape of the resonance. The model parameters are $A_{QD} = 0.15 \text{ eV}^2$, $A_{CNT} = 0.096 \text{ eV}^2$, and $M = 0.85$. We plug these parameters in the Eq. (7) and obtain the 110 meV Rabi splitting 2Ω . The CNTs exciton splits into two parts E^+ and E^- at 1.88 eV and for E^- is 1.76 eV, as determined by Eq. (6). The splitting energies are marked in Figure 4d by vertical red lines. The difference of the splitting energies results confirms the Rabi splitting $E^+ - E^-$ of 120 meV.

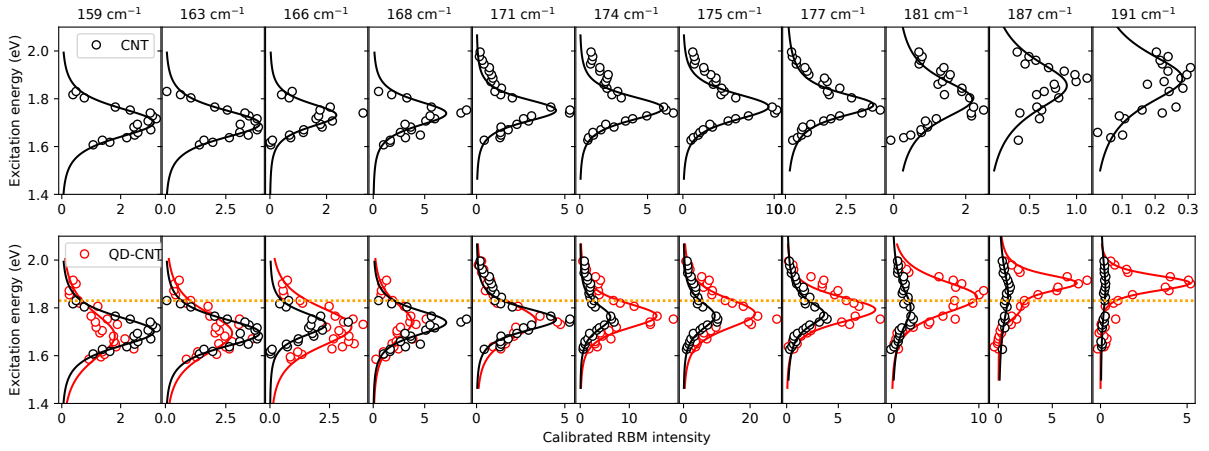


Figure 6: Resonant Raman profiles of the pristine and hybrid CNTs, with RBM frequencies indicated on the top. Top row with pristine CNTs, the symbols are experimental data and lines fits by Eq.(4), in bottom row RR profiles of pristine (black) are compared with QD-CNT-h (red), the lines are fits by Eq. (6) . The orange horizontal line represents the QD exciton energy E_{QD} .

The RR profiles experience systematic intensities increase and reduced broadening when the energies approach the QD energy. The RR profiles of the 11 pristine CNT chiralities are summarized in Figure 6 (top row). The lines represent fits by Eq.(4), the resonance maximum shift together with exciton resonance energies E_{CNT} . E_{CNT} increases with the RBM frequency as expected from a Kataura plot. The higher E_{CNT} the higher is the profile broadening, consistent with the previous observations in metallic CNTs. The RR profiles of the QD-CNT-h hybrids are compared with the pristine in the bottom row in Figure 6. In

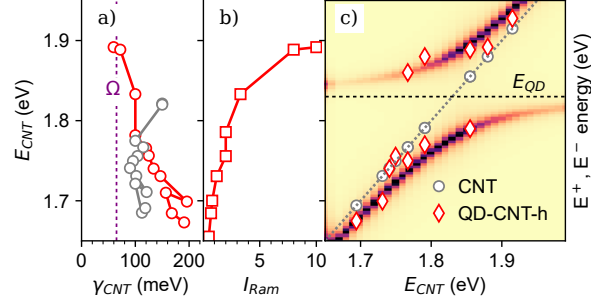


Figure 7: The effects of dd coupling between QD and CNT excitons. (a) Broadening factors (γ_{CNT}) extracted from the resonant Raman profiles (b) Raman enhancement calculated as a ratio between spectral weights of resonant Raman profiles $\frac{P_{QD-CNT}}{P_{CNT}}$. (c) Rabi splitting in the dipole-dipole coupling model. The circles represent E_{CNT} in the pristine system and diamonds the E^\pm in CNT-QD-h hybrid films. Dashed lines represent the energies of the uncoupled QD and CNTs.

the lowest energy CNT with RBM at 159 cm^{-1} we find a broader profile with overall smaller amplitude, however in the highest energy 191 cm^{-1} RBM we find up to 10 times stronger RR profile, compared to the pristine CNTs. It is nicely visible how the intensity increases and broadening decreases in hybrid system from left to right in Figure 6. The change of the broadening factors and Raman efficiencies are summarized in Figure 7b,c.

The RR shift caused by dd coupling depends on the energy difference between QD and CNT excitons. Figure 6 shows the resonant Raman profiles of 11 CNT chiralities. When E_{CNT} is lower than E_{QD} we find an overall red-shift of the resonance. The shift reverses to blue for the CNTs resonant above E_{QD} . When the E_{CNT} approaches E_{QD} , it splits into the $E_{+,-}$ parts. We fit the resonant Raman profiles from Figure 6 and determine $E_{+,-}$ energies. They are plotted in Figure 7a versus the energy of the uncoupled system E_{CNT} . At E_{QD} we find the gap equal to Rabi splitting 2Ω . The background of Figure 7a represents the $|\mu_{CNT}|$, with $2\Omega = 110\text{ meV}$. The experimental data points nicely overlay with the theoretical calculation. The broadening factors of the pristine CNTs are on average 120 meV and further increase for higher energy excitons, see Figure 7b. Each CNT chirality is coupled to QDs in the weak coupling regime, yet we are still able to resolve the coupling effects using dd altered resonant Raman spectroscopy.

Discussion

Dipole-dipole coupling between two excitonic states manifest in cross sections of resonant Raman scattering. These cross sections can be used to extract essential coupling parameters, such as Rabi splitting of the system. We believe that can be used in high variety of systems including Van der Walls two-dimensional³² and one-dimensional heterostructures.^{33,34} The optical states in the crystalline monolayers are often ruled by excitonic effects that will interact via dipole-dipole coupling mechanism. Further, the coupling strength can be enhanced by placing excitonic dipoles in mirror or plasmonic cavity. For instance in our design system with QDs and CNTs the coupling can be enhanced by using single chirality CNTs and a narrower distribution of QDs sizes, the Rabi frequency will scale \sqrt{N} , where N is the dipole density.

Conclusions

In conclusion we have introduced a Raman theory incorporating dipole-dipole coupling effects between excitons. A theoretical description is based on combination of perturbation theory and coupled oscillator model. This theory was experimentally verified in thin films containing the QD and nanotube mixture. The dd interactions between QD excitonic dipole perturbed the shape of the resonant Raman profiles of the CNTs. The resonance red or blue shifts depending on the relative energy between E_{QD} and E_{CNT} as predicted by our model. We further observe a decrease of effective broadening and increased Raman cross sections in the coupled system. In the future the dd altered Raman scattering can be implemented in many other low-dimensional hybrid excitonic systems.

Acknowledgement

Supporting Information Available

Additional figures are present in the Supporting information.

References

- (1) Mueller, N. S.; Okamura, Y.; Vieira, B. G.; Juergensen, S.; Lange, H.; Barros, E. B.; Schulz, F.; Reich, S. Deep strong light–matter coupling in plasmonic nanoparticle crystals. *Nature* **2020**, *583*, 780–784.
- (2) Boddeti, A. K.; Guan, J.; Sentz, T.; Juarez, X.; Newman, W.; Cortes, C.; Odom, T. W.; Jacob, Z. Long-Range Dipole-Dipole Interactions in a Plasmonic Lattice. *Nano Letters* **2022**, *22*, 22–28.
- (3) Davydov, A. S. The theory of molecular excitons. *Soviet Physics Uspekhi* **1964**, *7*, 145–178.
- (4) Nematiram, T.; Padula, D.; Troisi, A. Bright Frenkel Excitons in Molecular Crystals: A Survey. *Chemistry of Materials* **2021**, *33*, 3368–3378.
- (5) Pandya, R. et al. Microcavity-like exciton-polaritons can be the primary photoexcitation in bare organic semiconductors. *Nature Communications* **2021**, *12*, 6519.
- (6) Gu, J.; Ma, L.; Liu, S.; Watanabe, K.; Taniguchi, T.; Hone, J. C.; Shan, J.; Mak, K. F. Dipolar excitonic insulator in a moiré lattice. *Nature Physics* **2022**, *18*, 395–400.
- (7) Manjavacas, A.; Abajo, F. J. D.; Nordlander, P. Quantum plexcitonics: Strongly interacting plasmons and excitons. *Nano Letters* **2011**, *11*, 2318–2323.

- (8) Rödel, M.; Lisinetskaya, P.; Rudloff, M.; Stark, T.; Manara, J.; Mitric, R.; Pflaum, J. The Role of Molecular Arrangement on the Strongly Coupled Exciton–Plasmon Polariton Dispersion in Metal–Organic Hybrid Structures. *The Journal of Physical Chemistry C* **2022**, *126*, 4163–4171.
- (9) Davoodi, F.; Taleb, M.; Diekmann, F. K.; Coenen, T.; Rosnagel, K.; Talebi, N. Tailoring the Band Structure of Plexcitonic Crystals by Strong Coupling. *ACS Photonics* **2022**, *9*, 2473–2482.
- (10) Prasai, D.; Klots, A. R.; Newaz, A.; Niezgoda, J. S.; Orfield, N. J.; Escobar, C. A.; Wynn, A.; Efimov, A.; Jennings, G. K.; Rosenthal, S. J.; Bolotin, K. I. Electrical Control of near-Field Energy Transfer between Quantum Dots and Two-Dimensional Semiconductors. *Nano Letters* **2015**, *15*, 4374–4380.
- (11) Ernst, F.; Heek, T.; Setaro, A.; Haag, R.; Reich, S. Energy transfer in nanotube-*peryene* complexes. *Advanced Functional Materials* **2012**, *22*, 3921–3926.
- (12) Li, J.; Cushing, S. K.; Meng, F.; Senty, T. R.; Bristow, A. D.; Wu, N. Plasmon-induced resonance energy transfer for solar energy conversion. *Nature Photonics* **2015**, *9*, 601–607.
- (13) Rodarte, A. L.; Tao, A. R. Plasmon-Exciton Coupling between Metallic Nanoparticles and Dye Monomers. *Journal of Physical Chemistry C* **2017**, *121*, 3496–3502.
- (14) Araujo, P. T.; Doorn, S. K.; Kilina, S.; Tretiak, S.; Einarsson, E.; Maruyama, S.; Chacham, H.; Pimenta, M. A.; Jorio, A. Third and fourth optical transitions in semi-conducting carbon nanotubes. *Physical Review Letters* **2007**, *98*, 69.
- (15) Doorn, S. K.; Araujo, P. T.; Hata, K.; Jorio, A. Excitons and exciton-phonon coupling in metallic single-walled carbon nanotubes: Resonance Raman spectroscopy. *Physical Review B - Condensed Matter and Materials Physics* **2008**, *78*, 1–9.

- (16) Gordeev, G.; Jorio, A.; Kusch, P.; Vieira, B. G.; Flavel, B.; Krupke, R.; Barros, E. B.; Reich, S. Resonant anti-Stokes Raman scattering in single-walled carbon nanotubes. *Physical Review B* **2017**, *96*, 245415.
- (17) Yu, P. Y.; Cardona, M. *Fundamentals of Semiconductors – Physics and Materials Properties*; Springer, 1995.
- (18) Cardona, M.; Güntherodt, G. *Light Scattering in Solids II*. 1982.
- (19) Barker, A. S.; Hopfield, J. J. Coupled-Optical-Phonon-Mode Theory of the Infrared Dispersion in BaTiO₃, SrTiO₃, and KTaO₃. *Physical Review* **1964**, *135*, A1732–A1737.
- (20) Scott, J. F. Hybrid Phonons and Anharmonic Interactions in AlPO₄. *Physical Review Letters* **1970**, *24*, 1107–1110.
- (21) Hill, C.; Gordeev, G.; Guennou, M. Phonon-phonon coupling in bismuth vanadate over a large temperature range across the monoclinic phase. *arxiv:2306.05226* **2023**,
- (22) Thomas, R.; Thomas, A.; Pullanchery, S.; Joseph, L.; Somasundaran, S. M.; Swathi, R. S.; Gray, S. K.; Thomas, K. G. Plexcitons: The Role of Oscillator Strengths and Spectral Widths in Determining Strong Coupling. *ACS Nano* **2018**, *12*, 402–415.
- (23) Mueller, N. S.; Pfitzner, E.; Okamura, Y.; Gordeev, G.; Kusch, P.; Lange, H.; Heberle, J.; Schulz, F.; Reich, S. Surface-Enhanced Raman Scattering and Surface-Enhanced Infrared Absorption by Plasmon Polaritons in Three-Dimensional Nanoparticle Supercrystals. *ACS Nano* **2021**, *15*, 5523–5533.
- (24) Wroblewska, A.; Gordeev, G.; Duzynska, A.; Reich, S.; Zdrojek, M. Doping and plasmonic Raman enhancement in hybrid single walled carbon nanotubes films with embedded gold nanoparticles. *Carbon* **2021**, *179*, 531–540.

- (25) Brodu, A. et al. Exciton Fine Structure and Lattice Dynamics in InP/ZnSe Core/Shell Quantum Dots. *ACS Photonics* **2018**, *5*, 3353–3362.
- (26) Rafipoor, M.; Tornatzky, H.; Dupont, D.; Maultzsch, J.; Tessier, M. D.; Hens, Z.; Lange, H. Strain in InP/ZnSe, S core/shell quantum dots from lattice mismatch and shell thickness - Material stiffness influence. *Journal of Chemical Physics* **2019**, *151*.
- (27) Seong, M. J.; Mičić, O. I.; Nozik, A. J.; Mascarenhas, A.; Cheong, H. M. Size-dependent Raman study of InP quantum dots. *Applied Physics Letters* **2003**, *82*, 185–187.
- (28) Elamathi, M.; Peter, A. J.; Lee, C. W. Role of various dielectric environment matrices of InP/ZnS core/shell quantum dot on optical gain coefficient. *European Physical Journal D* **2020**, *74*.
- (29) Vossmeier, T.; Katsikas, L.; Giersig, M.; Popovic, I. G.; Diesner, K.; Chemseddine, A.; Eychmüller, A.; Weller, H. CdS nanoclusters: Synthesis, characterization, size dependent oscillator strength, temperature shift of the excitonic transition energy, and reversible absorbance shift. *Journal of Physical Chemistry* **1994**, *98*, 7665–7673.
- (30) Mičić, O. I.; Jones, K. M.; Cahill, A.; Nozik, A. J. Optical, electronic, and structural properties of uncoupled and close-packed arrays of inP quantum dots. *Journal of Physical Chemistry B* **1998**, *102*, 9791–9796.
- (31) Maultzsch, J.; Telg, H.; Reich, S.; Thomsen, C. Radial breathing mode of single-walled carbon nanotubes: Optical transition energies and chiral-index assignment. *Physical Review B - Condensed Matter and Materials Physics* **2005**, *72*, 205438.
- (32) Geim, A. K.; Grigorieva, I. V. Van der Waals heterostructures. *Nature* **2013**, *499*, 419–425.
- (33) Guo, J.; Xiang, R.; Cheng, T.; Maruyama, S.; Li, Y. One-Dimensional van der Waals Heterostructures: A Perspective. *ACS Nanoscience Au* **2022**, *2*, 3–11.

- (34) Gordeev, G.; Wasserroth, S.; Li, H.; Flavel, B.; Reich, S. Moiré-Induced Vibrational Coupling in Double-Walled Carbon Nanotubes. *Nano Letters* **2021**, *21*, 6732–6739.